

Effects of the Material Structure on the Catalytic Activity of Peptide-Templated Pd Nanomaterials

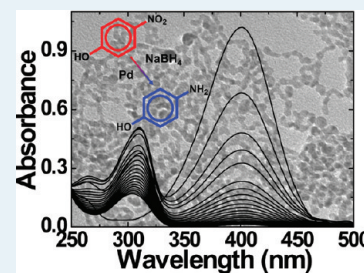
Rohit Bhandari and Marc R. Knecht*

Department of Chemistry, University of Kentucky, 101 Chemistry-Physics Building, Lexington, Kentucky 40506-0055, United States

Supporting Information

ABSTRACT: Bioinspired approaches represent emerging methods for the fabrication and application of nanomaterials under desirable ambient conditions. By adapting biomimetic processes to technological applications such as catalysis, new directions could be achieved for materials that are reactive under energy efficient and ecologically friendly conditions. Such materials have been prepared using a self-assembling peptide template in which non-spherical Pd nanostructures can be generated. Based upon the Pd/peptide ratio, different inorganic morphologies can be prepared within the peptide scaffolds, including nanoparticles, linear nanoribbons, and complex nanoparticle networks (NPNs). These materials are catalytically reactive; however, the effects of the template and Pd morphology remain poorly understood. To ascertain these effects, we present an in depth catalytic analysis of the bioinspired peptide-based system using two vastly different reactions: Stille C–C coupling and 4-nitrophenol reduction. For all of the systems studied, enhanced reactivity was observed for the Pd nanoparticles and NPNs over the nanoribbons. This effect is suggested to arise from two key structural characteristics of the materials: the amount of inorganic surface area and the penetration depth within the peptide scaffold. Such results are important for the design and development of selective nanocatalytic systems, where the composite structure works in conjunction to mediate the overall activity.

KEYWORDS: nanocatalysis, bioinspired nanotechnology, Pd, peptides, Stille coupling, 4-nitrophenol reduction



INTRODUCTION

A tremendous amount of research has been focused upon noble metal nanoparticles because of their numerous applications ranging from catalysis^{1–7} to energy production/storage^{8–12} to biomedical diagnostics.^{13–16} These materials gain their high degree of functionality from their inherent properties, which are typically a function of their size, shape, and composition.^{17,18} Various nanostructures have been produced for catalytic applications, from which their three-dimensional morphology plays a key role in their functionality. To fabricate stable and reactive nanocatalysts, ligands must be present that passivate the surface to prevent bulk material aggregation of the inorganic component. Typically, these ligands bind to the nanoparticle surface, where either electrostatic repulsion or steric effects stabilize the materials.^{17–19} Unfortunately, binding of the ligands directly to the nanoparticle surface can significantly hinder access to the inorganic component, which could diminish or prevent reactivity. This factor is critically important for nanocatalysts where the reagents must come in direct contact with the metal, typically Pd or Pt, to drive the reaction.^{17,20–23} To overcome this effect, various materials synthetic routes have been derived to maximally expose the inorganic surface of the nanoparticle.⁴ For instance, bulky ligands such as peptides and branching dendrons have been employed^{1,3,24} where the steric bulk and surface binding modes of these ligands results in greater inorganic exposure as compared to standard alkane thiols.²⁵ Other methods have employed templates

to generate the inorganic nanostructure within an organic scaffold,^{2,4,21,22} which does not require covalent surface binding of the inorganic component for stability.^{26–28} Such template-based materials are promising for catalytic applications and may allow for desirable reagent selectivity; however, the effect of the actual template on the catalytic process remains unclear.

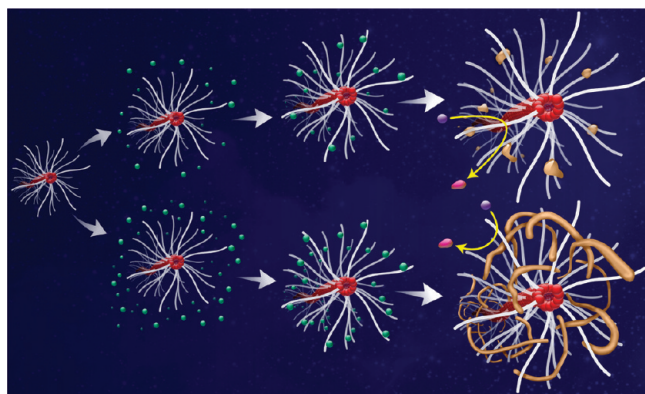
A variety of templates have been used for the production of catalytically reactive Pd nanomaterials including dendrimers,^{4,29} polymers,^{30,31} peptides,² and micelles.^{32–34} Employing Pd as the inorganic component is ideal because of its high degree of reactivity for a wide variety of catalytic reactions ranging from C–C coupling^{1–3,17,20,35–38} to hydrogenation.^{4,21,22,24,33,37,39} For these template-based materials, the inorganic components are wholly contained within the organic framework to prevent bulk aggregation. To that end, Pd ions, typically Pd²⁺ or Pd⁴⁺, are sequestered within the scaffold that, upon reduction, forms the metallic nanomaterial. From this structure, the exterior template is likely to play a significant role in the reactivity of the material such that it could allow for selectivity based upon the size, composition, and polarity of the catalytic reagents.⁴⁰ As such, the organic framework may act as a size or composition selective gate, thus allowing only certain molecules access to the reactive surface, which is ideal for reactions with multiple substrates. Furthermore, the

Received: November 22, 2010

Revised: December 13, 2010

Published: January 18, 2011

Scheme 1. Synthetic Scheme Employed to Prepare the Pd Nanomaterials within the Biomimetic Template^a

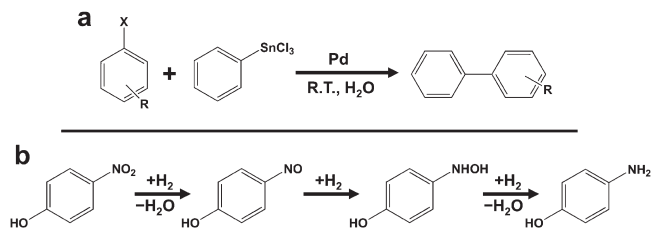


^aThe top pathway employs a low Pd/peptide ratio to result in Pd nanoparticles, while the bottom pathway possesses a higher Pd/peptide ratio to prepare Pd NPNs. In the scheme, the green spheres represent Pd²⁺ ions that complex to the peptide template, which, upon reduction, form the zerovalent Pd nanomaterials.

template may also play a role in controlling the reaction rate; by having a complex structure, the reagents must penetrate through the organic scaffold, react at the metallic component, and then traverse back through the template for release to solution.^{2,40} Unfortunately, it is difficult to accurately probe such template-based effects because the structural morphology of nanocatalysts prepared via these routes is typically limited. To fully ascertain these effects, it would be advantageous to employ a template-based synthetic approach that allows for a significant degree of structural control over both the catalytic component depth within the template and the reactive surface area.

Bioinspired materials^{41,42} have recently been developed for the generation of precisely controlled nanostructures that serve as highly reactive catalysts,^{1–3,43,44} efficient Li-ion batteries,^{8–10} and sensitive biobased sensors.⁴⁵ Such highly promising materials are attractive as they operate under energy efficient and environmentally benign conditions,^{41,42} thus enhancing their range of use. We have recently demonstrated a bioinspired approach to the production of nanocatalysts using a peptide template,² as shown in Scheme 1. The template employs the R5 peptide (SSKKSYSYSGSKGSKRRIL) isolated from the diatom *Cylindrotheca fusiformis* for the production of biosilica.^{46,47} Previous studies have demonstrated that the R5 is able to self-assemble from the C-terminal RRIL motif to generate large peptide frameworks on the order of ~800 nm.⁴⁸ Using this biomimetic template, catalytically reactive Pd nanostructures of three different morphologies can be prepared based upon the Pd/peptide ratio employed during the synthesis; spheres, ribbons, and nanoparticle networks (NPNs) can be fabricated using a ratio of 60, 90, and 120, respectively.² Preliminary evidence suggests that the individual structures are able to drive Stille coupling, shown in Scheme 2a,^{49,50} which forms a C–C bond between an aryl halide and an organostannane in water at room temperature using low Pd loadings. The turnover frequency (TOF) of the three differently shaped systems was suggested to be a function of the Pd surface area and the reagent penetration depth required to reach the reactive surface. These two factors are likely the result of the composite structure of the materials;² however, additional in depth studies are required to confirm this

Scheme 2. Catalytic Reactions Employed to Probe the Structure/Function Relationship of the Peptide-Templated Pd Nanomaterials: (a) Stille Coupling and (b) 4-Nitrophenol Reduction



unique reactivity to determine if these structural attributes universally effect the catalytic reactivity of template-based materials. Interestingly, by using these unique peptide templates, the reagent penetration depth to reach the Pd surface and the Pd surface area can be tuned by the Pd/peptide ratio. Such structural control is difficult to achieve using other template-based materials, thus suggesting that the peptide templated structures are positioned well for catalyst structural studies.

Here we present an in depth analysis of the effects of the peptide scaffold on the catalytic reactivity of the Pd nanomaterials prepared within the biomimetic template. Based upon the structure and synthetic methods, shown in Scheme 1, we find that the amount of surface area and the penetration depth to reach the inorganic surface vary based upon the Pd loading within the peptide template. To that end, the Pd nanoparticles produced at a Pd/peptide ratio of 60 (termed Pd60) possess the largest metallic surface area; however, they are highly dispersed within the scaffold and have the largest reagent penetration depth. As the Pd morphology changes to the NPNs prepared at a ratio of 120 (termed Pd120), the surface area decreases; however, the reactive Pd materials are pushed closer to the template surface, thus significantly minimizing their depth within the peptide framework.² As a result, the reactive Pd materials are closer to the scaffold/solution interface for more rapid interactions with the reagents. By enhancing one of these two structural criteria, the Pd60 and Pd120 materials demonstrate maximal reactivity; however, for the nanoribbons prepared with a Pd/peptide ratio of 90 (termed Pd90), both structural factors are diminished. For these materials, the reactive surface area is lower than the Pd60 nanospheres and the penetration depth is greater than the Pd120 NPNs, thus lower catalytic activity is observed. These effects were probed using two different catalytic reactions: Stille coupling and 4-nitrophenol reduction, both of which are presented in Scheme 2. These two reactions were specifically chosen as they follow significantly different catalytic pathways, thus allowing for a complete analysis of the effects of reaction mechanism and the catalyst composite structure. Furthermore, by studying 4-nitrophenol reduction, an in depth reaction analysis can be completed to kinetically isolate the two structural effects that likely play a significant role in the reactivity. These results are important for three key factors. First, they expand the degree of reactivity for biomimetic and peptide-based materials toward new and important catalytic reactions. Second, these results demonstrate that highly reactive structures can be generated in various morphologies for reactivity under eco and energy efficient conditions that cannot typically be employed. Third, critical catalytic and structural factors for template-based materials are

demonstrated that could be used to tune the reactivity and selectivity of nanocatalysts. As a result, key structure–function relationships are elucidated that may play a significant role in future nanocatalyst structural design.

EXPERIMENTAL SECTION

Chemicals. K_2PdCl_4 , 4-biphenylcarboxylic acid, 4-*t*-butylphenol, 4-iodophenol, and 4-bromobenzoic acid were purchased from Sigma Aldrich, while 3-iodobenzoic acid and 4-nitrophenol were acquired from Acros Organics. 4-Chlorobenzoic acid, 4-bromophenol, and 4-chlorophenol were purchased from TCI America. $NaBH_4$ was purchased from EMD chemicals, while dimethylformamide (DMF), methanol, and acetonitrile were purchased from Pharmaco-Aaper. Fmoc protected amino acids and WANG resins for the synthesis of the R5 peptide were purchased from Advanced Chemtech (Louisville, KY). All materials and solvents were used as received. Eighteen $M\Omega$ cm water (Millipore; Bedford, MA) was used for all experiments.

Characterization. UV–vis analysis was conducted on an Agilent 8453 UV–vis spectrometer employing a 1.00 cm path length quartz cuvette (Starna). Transmission electron microscopy (TEM) was performed using a JEOL 2010F electron microscope operating at 200 kV with a resolution of 0.19 nm. All samples were prepared on 400 mesh carbon coated Cu grids (EM Sciences), where 5.00 μ L of the reaction solution was pipetted onto the grid surface and allowed to dry in a desiccator.

Peptide-Template Synthesis of Pd Nanostructures. The R5 peptide was synthesized using standard automated Fmoc procedures⁵¹ on a TETRAS peptide synthesizer (CreoSalus; Louisville, KY). All peptides were purified by HPLC and confirmed via Matrix-Assisted Laser Desorption/Ionization-Time of Flight (MALDI-TOF) analysis. For the synthesis of the Pd nanostructures, the production of spherical nanoparticles is described using a Pd/peptide ratio of 60; however, identical procedures were employed that increased the Pd/peptide ratios to prepare the non-spherical structures. Initially, 4.93 μ L of a 4.97 mM (10 mg/mL) R5 peptide stock solution in water was added to 3.00 mL of deionized water. To this solution, 14.7 μ L of 100 mM K_2PdCl_4 was added to achieve a Pd/peptide ratio of 60. For Pd/peptide ratios of 90 and 120, 22.05 and 29.39 μ L of the K_2PdCl_4 stock solution were added, respectively. The solution was allowed to stir vigorously for 15.0 min and then 75.0 μ L of a freshly prepared 0.10 M $NaBH_4$ solution was added to reduce the materials to zerovalent Pd. The materials were allowed to reduce for 1.00 h to ensure complete reduction. The solution was then dialyzed using cellulose dialysis tubing (14 kDa cutoff) against water for 24.0 h.

Catalytic Stille Coupling. The Pd nanomaterials were employed as catalysts for the Stille reaction using standard methods.^{1–3} Here, different aryl halides that varied the halogen position and identity were coupled with phenyltin trichloride ($PhSnCl_3$) to generate their respective biphenyl product. For these reactions, 0.50 mmol of the aryl halide and 0.60 mmol of $PhSnCl_3$ were dissolved in 8.00 mL of 2.25 M KOH. Under vigorous stirring, the Pd nanomaterials were added to the reaction at a Pd loading of 0.050 mol %. The reactions were then allowed to proceed for 24.0 h in air. Once completed, the reactions were quenched with 50.0 mL of 5.00% HCl, the product was extracted three times using diethyl ether, and finally washed with a saturated NaCl solution. The product in the ether layer was then dried using Na_2SO_4 , to which 0.50 mmol of the internal standard was added (*t*-butylphenol for carboxylic acid substrates and 4-biphenylcarboxylic acid for phenol substrates). The ether was subsequently evaporated using a rotary evaporator and then a small amount of product was dissolved in deuterated chloroform and characterized using a 400 MHz NMR spectrometer.

For the TOF analysis, the reaction was scaled up 5 fold to a final volume of 40.5 mL. Immediately after catalyst addition, a 4.00 mL

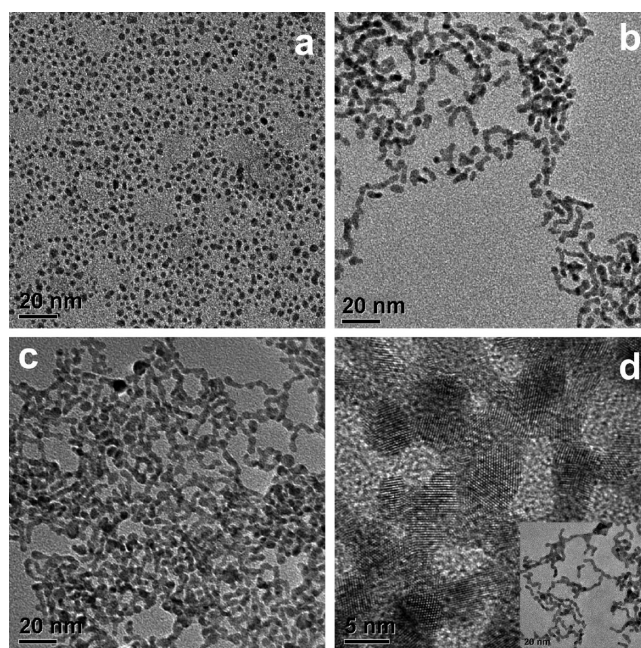


Figure 1. TEM images of the materials fabricated using the peptide template employing Pd/peptide ratios of (a) 60, (b) 90, and (c) 120. Panel (d) presents a high-resolution image of the NPNs prepared with a ratio of 120 demonstrating their polycrystalline structure. The inset of panel (d) presents a TEM image of a dispersed sample of NPNs.

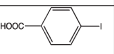
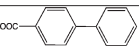
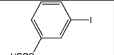

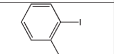

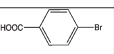
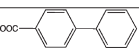
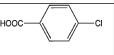
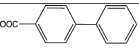
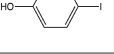
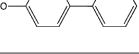

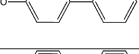
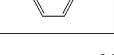
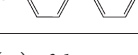
aliquot was extracted and quenched, after which subsequent aliquots were extracted and quenched every 60.0 min. Once finished, the product yield in each aliquot was quantitated from which the TOF was determined using standard methods.^{1–3}

Reduction of 4-Nitrophenol. The catalytic reduction of 4-nitrophenol to 4-aminophenol was modeled on previous literature precedent.^{52,53} Briefly, in separate quartz cuvettes, 500 μ L of the Pd60 sample, 335 μ L of the Pd90 sample, and 250 μ L of the Pd120 sample solution were added to the reaction, to which 500 μ L of a 63.0 mM $NaBH_4$ solution was added to ensure complete reduction of the Pd materials. These values of the Pd materials were selected to ensure the same Pd concentration for all reactions (79.0 μ M), regardless of the Pd shape. Additionally, sufficient water was added to reach a volume of 1.00 mL. The solution was then left undisturbed for 15.0 min, after which 2.00 mL of an 85.0 μ M aqueous 4-nitrophenol solution was added. Immediately after substrate addition, time dependent absorption spectra were recorded at 7.00 s intervals for 5.00 min at temperatures between 10.0 and 60.0 $^{\circ}C$. All spectra were background subtracted against a solution of the appropriate Pd nanomaterials and $NaBH_4$ at the reaction concentrations in water. Triplicate reactions were studied from which statistical analysis of the reactivity could be extracted.

RESULTS AND DISCUSSION

Synthesis and Characterization of the Pd Nanomaterials. The Pd materials used for the catalytic analysis were prepared in a simple two-step process in water.² When the R5 peptide is dissolved in aqueous solution, it is able to self-assemble and form aggregates on the order of \sim 800 nm,⁴⁸ resulting in localized areas of amines. These structures are then used to template the production of Pd nanomaterials of different morphologies ranging from spheres to NPNs. In the first step, Pd^{2+} ions are introduced to the peptide template, from which complexation of the metal ions to the peptide amines is possible. As a result, the

Table 1. Stille Coupling Results Employing the Pd60 Nanospheres, Pd90 Nanoribbons, and Pd120 NPNs^a

Aryl Halide	Product	Pd60	Pd90	Pd120
		100 (452 ± 16)	100 (334 ± 38)	100 (437 ± 14)
		48.4 ± 0.8 (244 ± 4.4)	50.9 ± 2.9 (221 ± 16)	46.9 ± 2.4 (237 ± 15)
		0	0	0
		19.4 ± 0.9 (17.9 ± 3.2)	21.9 ± 5.8 (16.1 ± 0.5)	29.2 ± 9.6 (18.4 ± 3.6)
		2.3 ± 0.6	0.85 ± 0.08	1.4 ± 0.6
		75.9 ± 8.9 (141 ± 9.4)	70.5 ± 3.6 (122 ± 18)	68.9 ± 3.0 (135 ± 1.4)
		9.7 ± 4.6 (5.8 ± 2.1)	6.5 ± 1.3 (3.3 ± 0.9)	5.6 ± 1.0 (4.0 ± 0.7)
		0	0	0

^a Percent yield (%) of the anticipated product are listed above the TOF value for the individual reactions, which are shown in parentheses. Reaction conditions: 1.0 equiv. of aryl halide, 1.2 equiv. of PhSnCl₃, 0.05 mol % Pd, 8.0 mL of 2.25 M KOH, 25 °C, *t* = 24.0 h.

Pd²⁺ is extracted from the solution and sequestered within the biological scaffold. In the second step, the metal ions are reduced using a significant excess of NaBH₄. This causes the formation of zerovalent Pd nanomaterials of various morphologies and depths within the assembled peptide framework as dictated by the amount of metal loaded within the template.

Figure 1 presents a TEM analysis of the Pd materials prepared with a Pd/peptide ratio of 60, 90, and 120, termed the Pd60, Pd90, and Pd120 samples, respectively. For the Pd60 materials, spherical nanoparticles with a size distribution of 2.6 ± 0.5 nm were generated, which is similar to previous results.² For the Pd90 and Pd120 materials, shown in Figures 1b and c, respectively, non-spherical structures that possessed a linear morphology were generated. For the Pd90 sample, nanoribbon like materials were prepared, while for the Pd120 sample, NPNs were achieved that possessed a high degree of inorganic branching. Figure 1d presents a high-resolution image of the NPNs that displays lattice fringes with *d* spacings of 2.5 Å and hexagonal atomic arrays, both of which are consistent with the face-centered cubic structure of Pd. Additionally, the inset of Figure 1d presents a medium resolution micrograph of a low-density region of the NPNs demonstrating their linear and branching morphology.

The structural effects of the template control the morphology of the inorganic materials, as shown in Scheme 1. To that end, the peptide structure possesses numerous amines distributed within the scaffold that can greatly disperse the Pd²⁺ ions throughout the template. As a result, when a Pd/peptide ratio of 60 is used, the metal ions are separated by greater distances as compared to when a ratio of 120 is employed that more fully loads the peptide framework. Upon reduction, Pd nanoparticles nucleate within the scaffold where the average distance between the particles varies based upon the metal loading; at lower ratios, the distance between the particles is quite large, while for the higher loadings,

smaller interparticle distances are produced. At the lower ratios, the particle distance is large enough to prevent aggregation; however, at the higher ratios, the particles are close enough to allow for their specific aggregation in a linear fashion because of the steric effects of the branches of the peptide framework. As numerous particles begin to linearly aggregate, formation of the networked morphology occurs to generate the final NPN structure. The networked arrangement is produced via the formation of branching points within the inorganic component because of the organization of multiple particles at a single location. The degree of linear network formation is controlled by the amount of Pd within the template such that as the ratio decreases, lesser aggregation is anticipated until no aggregation occurs as observed for the Pd60 spherical particles.

Effects of the Peptide Template on the Stille Coupling Reaction. The catalytic reactivity of nanomaterials is controlled by the three-dimensional structure, which mediates the interactions of substrates with the active surface.^{1–4,17,20,22,36,39} It is critical that the structure–function relationship of these materials be determined, which could be used in the future design of enhanced systems that meet next generation reactivity demands, where template-based materials such as those of the present study may make significant contributions. A set of important reactions that follow very similar mechanisms are those of C-couplings, which have recently been shown to have the potential to operate under optimized energy and environmental conditions using Pd nanoparticle catalysts.¹⁷ Of these reactions, Stille coupling, shown in Scheme 2a, is extensively used to achieve the formation of C–C bonds.^{49,50} For this reaction, the aryl halide is able to oxidatively add to a Pd⁰ catalyst that then positions the nucleophile of the tin complex onto the Pd²⁺ species via a transmetalation step. Finally, through reductive elimination, the C–C bond is formed while the Pd⁰ catalyst is regenerated. As has been preliminarily shown for a single reaction, the peptide templated Pd nanospheres, nanoribbons, and NPNs are catalytically active for the Stille coupling of 4-iodobenzoic acid with PhSnCl₃ to produce biphenylcarboxylic acid in high yields at low Pd loadings on the order of 0.005 mol % Pd.² These materials previously demonstrated TOF values for this specific reaction, which are included in Table 1 and Figure 2, of 452 ± 16 mol product (mol Pd × h)^{–1} for the Pd60 sample, 334 ± 38 mol product (mol Pd × h)^{–1} for the Pd90 nanoribbons, and 437 ± 14 mol product (mol Pd × h)^{–1} for the NPNs prepared in the Pd120 system.² While this single reaction indicates that the materials are catalytically active, the aryl halide composition and identity can also alter the catalytic reactivity, which is relatively unknown for non-spherical templated materials. Furthermore, the effects of the template may also be related to the reagent composition; thus, studies of the reactivity as a function of reagent identity are required.

When the chemical structure of the aryl halide is altered, significant shifts in the reactivity of the materials are observed. For instance, when 3-iodobenzoic acid is employed as the starting material, lower product yields are achieved as compared to the 4-iodobenzoic acid species, as shown in Table 1. Employing the Pd60 sample, product yields of 48.4 ± 0.8% were achieved in 24.0 h using a Pd loading of 0.050 mol %. When the Pd90 and Pd120 materials catalyzed the reaction, product yields of 50.9 ± 2.9% and 46.9 ± 2.4%, respectively, were achieved. Overall, this represents an approximately 2-fold decrease in the product yield with a switch of the halide position from 4 to 3 in the benzoic acid structure. This trend in decreasing

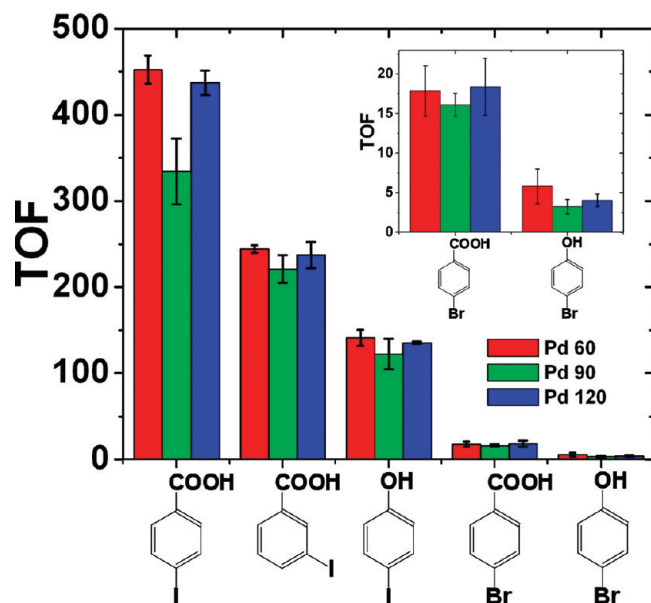


Figure 2. TOF analysis of the Stille coupling reaction employing the selected aryl halides that probe reagent structural effects. Note that for every reaction, the Pd90 materials demonstrate a lower TOF value, on average, as compared to the Pd60 and Pd120 materials.

product yields continued with 2-iodobenzoic acid such that no product was observed when any of the shaped Pd nanomaterials were employed to catalyze the reaction, consistent with other comparable catalysts.^{3,20} Such a trend is likely the result of the atomic structure of the aryl halide, suggesting that the positioning of the functional groups within the reagent plays an important role in the reactivity of the templated Pd nanomaterials.

When the halogen was altered from I to Br or Cl on the benzoic acid reagent, varied reactivity was observed that followed specific trends.^{49,50} For instance, using 4-bromobenzoic acid resulted in decreased product yields of $19.4 \pm 0.9\%$, $21.9 \pm 5.8\%$, and $29.2 \pm 9.6\%$ for the reactions catalyzed by the Pd60, Pd90, and Pd120 materials, respectively, over 24.0 h at room temperature with a loading of 0.050 mol % Pd. Such reactivity was somewhat surprising as bromo-based reagents typically produce negligible product amounts under such conditions.³ Even more remarkable, product yields were observed for 4-chlorobenzoic acid. For this reagent, product yields of $2.3 \pm 0.6\%$ were observed for the Pd60 nanospheres, while yields of $0.85 \pm 0.08\%$ and $1.4 \pm 0.6\%$ were noted for the Pd90 nanoribbons and Pd120 NPNs, respectively. While the product yields are quite low because of the Cl group, they suggest that Pd nanoparticles could drive the Stille coupling of chlorinated aryl halides that has proven to be challenging.^{3,17,20} Together, the effects of the halide identity indicate maximal yields are achieved for I containing species and decreasing yields are achieved for reagents with lighter halogens, which is consistent with known trends in C-coupling schemes.^{3,17,20,49,50}

Further analysis of the aryl halide structure focused on the individual functional group of the reagent. It is known that the rate of Stille coupling can be modulated by the electronic character of the aryl halide,⁴⁹ thus changes in the molecular composition can significantly affect the reactivity. As a result, by changing the benzoic acid substrate to a phenol-based system, significant changes to the molecular electronics occurs, which can be observed in the catalytic results. For instance, when using

4-iodophenol, the product yields decreased to $75.9 \pm 8.9\%$, $70.5 \pm 3.6\%$, and $68.9 \pm 3.0\%$ for the Pd60, Pd90, and Pd120 materials, respectively, as compared to 4-iodobenzoic acid, over the 24.0 h reaction time. Furthermore, similar trends in the halide identity were observed for the halogenated phenols as compared to the acid-based reagents. Using 4-bromophenol, yields of the coupled product diminished to $9.7 \pm 4.6\%$ for the Pd60 materials, while $6.5 \pm 1.3\%$ was determined for the Pd90 nanoribbons and $5.6 \pm 1.0\%$ was quantitated for the NPNs under identical reaction conditions. For 4-chlorophenol, no product was detected for any of the materials, consistent with observed trends in changes to both the functional group and halogen. Taken together, these results suggest that multiple characteristics of the aryl halide reagents work in combination to modulate the C-coupling reactivity of the peptide-templated materials, including functional group orientation, electronic character, and halogen identity.

While the actual product yields are indicative of the catalytic reactivity, the TOF values associated with each template-based nanomaterial represents a more quantitative analysis of the catalytic capability and could reflect differences associated with the complex composite structure. When considering the benzoic acid aryl halides, the highest TOF values are observed for 4-iodobenzoic acid² that decrease with changes to the halogen identity and functional group position. This follows the trend that was observed above with the product yields, and is shown in Figure 2. For instance, when using 3-iodobenzoic acid, TOF values of 244 ± 4.4 mol product $(\text{mol Pd} \times \text{h})^{-1}$, 221 ± 16 mol product $(\text{mol Pd} \times \text{h})^{-1}$, and 237 ± 15 mol product $(\text{mol Pd} \times \text{h})^{-1}$ were observed for the Pd60, Pd90, and Pd120 materials, respectively. These values are lower than those previously reported for the 4-iodobenzoic acid species² and are consistent with the decreased product yields. No TOF analysis could be completed for 2-iodobenzoic acid because of its lack of activity. When the halogen identity was altered to Br in 4-bromobenzoic acid, significantly lower TOFs were observed as anticipated because of the low product yields that were detected. For this reagent, the Pd60 nanospheres demonstrated a TOF of 17.9 ± 3.2 mol product $(\text{mol Pd} \times \text{h})^{-1}$, while the Pd90 nanoribbons possessed a value of 16.1 ± 0.5 mol product $(\text{mol Pd} \times \text{h})^{-1}$. For the highly integrated NPNs, a TOF of 18.4 ± 3.6 mol product $(\text{mol Pd} \times \text{h})^{-1}$ was observed using the bromo-based acid reagent. These low values are consistent with the minimized product yields, which are likely attributed to the halogen identity and its effects on the reaction mechanism and degree of reactivity. While product generation was observed for the 4-chlorobenzoic acid species, further TOF analysis was not conducted because of the extremely low product amounts over the 24.0 h time period.

When TOF analyses were conducted for the phenol-based substrates, lower values were observed as compared to the benzoic acid reagents. When using 4-iodophenol, TOF values of 141 ± 9.4 mol product $(\text{mol Pd} \times \text{h})^{-1}$, 122 ± 18 mol product $(\text{mol Pd} \times \text{h})^{-1}$, and 135 ± 1.4 mol product $(\text{mol Pd} \times \text{h})^{-1}$ were observed for the Pd60, Pd90, and Pd120 nanomaterials, respectively. When 4-bromophenol was studied, the values were significantly lowered to 5.8 ± 2.1 mol product $(\text{mol Pd} \times \text{h})^{-1}$ for the Pd nanospheres fabricated from the Pd60 sample, while the Pd90 nanoribbons and Pd120 NPNs demonstrated TOFs of 3.3 ± 0.9 mol product $(\text{mol Pd} \times \text{h})^{-1}$, and 4.0 ± 0.7 mol product $(\text{mol Pd} \times \text{h})^{-1}$, respectively. Again, no reactivity was observed for the 4-chlorophenol reagent; therefore, a TOF analysis was unable to be conducted.

The results gained from the Stille analysis suggest key reagent composition and catalyst structural motifs that are important for the design of template-based nanocatalysts. For instance, the identity and position of the functional groups within the ring structure of the aryl halide directly impact the reaction. To that end, reagents that possess an electron-withdrawing group, such as the benzoic acid reagents, demonstrated higher reactivity and TOF values as compared to their counterparts that possess electron donating hydroxyl groups of the phenol compounds. Furthermore, the halogen species played a critical role in the functionality such that as lighter halogens were used, the reactivity of the system decreased. These observations follow previously observed trends in reactivity for the aryl halide reagents when employing traditional organometallic catalysts.^{49,50} Such effects are likely to mediate both the oxidative addition and transmetalation steps to alter the reactivity; however, the structure of the inorganic materials and the actual nanoparticle-based mechanism could also play a significant role in the reactivity. At present, a unique atom leaching mechanism has been proposed for C-coupling reactions employing Pd nanoparticle catalysts.^{1,17,35,54,55} In this mechanism, during the oxidative addition step, Pd²⁺ ions are leached from the nanomaterial surface from which the reaction is driven in solution. Upon completion, the regenerated Pd atoms either recombine with the remaining nanomaterials or form bulk Pd black, which is catalytically inactive and precipitates from solution. In this approach, alterations in the particle structure, size, and distribution are anticipated; however, full analytical determination of the actual mechanism remains challenging because of the limited techniques available to probe particles on this size scale at the dilute concentrations. Interestingly, when these reactions are run at relatively high template catalyst loadings, ≥ 0.10 mol % Pd, a black precipitate is observed that suggests the atom leaching mechanism is responsible for the reactivity.

While aryl halide oxidative addition at the Pd surface is the likely cause of Pd leaching, the reactions are processed in air, thus chloride-assisted oxidation of the Pd materials in the presence of O₂ could drive the leaching process. To minimize this effect, the nanocatalysts were dialyzed to remove excess Cl⁻ prior to the reaction; however, PhSnCl₃ is used as the transmetalation reagent. To confirm that aryl halide oxidative addition controls Pd leaching, Stille coupling of 4-iodobenzoic acid with PhSnCl₃ was catalyzed by the Pd60 nanospheres under N₂ at a loading of 0.10 mol % Pd. Here, quantitative product yields were achieved in 24.0 h under conditions that disfavor chloride-based oxidation, thus suggesting oxidative addition of the aryl halide does indeed drive Pd leaching.

Based upon these controls and results, for the present peptide-template-based Pd nanocatalysts, oxidative addition at the inorganic surface is likely required for reaction initiation via Pd-leaching; thus, the Pd surface area is involved in the reactivity. For this, the reagents must penetrate into the peptide scaffold, locate, react, and extract Pd²⁺ from the inorganic surface, drive the Stille coupling, and finally diffuse out of the peptide template. To that end, a higher surface-to-volume ratio would expose more of the reactive metal to the reagents, thus allowing for a more rapid abstraction process and thus increasing the TOF of the system. Furthermore, the positioning of the functional groups within the ring structure may impede oxidative addition.^{3,20} For instance, employing the 2-iodobenzoic acid substrate, the halogen and carboxylic acid functionalities are closely spaced that upon oxidative addition at the inorganic surface, the acid group will

be appropriately positioned for interactions with the Pd. As a result, two points of chemical interaction occur, which results in stronger surface adsorption. This effect likely prevents or inhibits oxidative addition and/or the leaching process to result in no catalytic turnover as previously demonstrated using smaller spherical nanoparticles.^{3,20} When 3-iodobenzoic acid was employed, reactivity was observed; however, lower yields and TOF values were determined as compared to 4-iodobenzoic acid. While the functional groups are further separated as compared to 2-iodobenzoic acid, this spacing is lower as compared to 4-iodobenzoic acid. As a result, some additional degree of interaction with the extended one-dimensional Pd nanomaterials is likely to occur with the 3-iodobenzoic acid species. Previous results using peptide-capped or dendrimer-encapsulated Pd nanoparticles were able to achieve quantitative yields for this reagent;^{3,20} however, the nanoparticles used for these previous studies were smaller and were exclusively spherical as compared to the larger and non-spherical materials of the present study. By having the larger and/or linear nanostructures, the Pd surface area in the immediate vicinity of the oxidative addition site is larger. From this, the ability for the carboxylic acid group of 3-iodobenzoic acid to interact with the metallic material is enhanced to lead to adsorption that partially inhibits Pd²⁺ leaching. As a result, less Pd species could be leached from the inorganic surface to drive the reaction, thus lowering the yields and TOF values. Based upon this hypothesis, it would be anticipated that the interaction strength of the aryl halide with the Pd surface would follow a trend $4 < 3 < 2$, where these numbers represent the position of the halogen group with respect to the acid moiety. Interestingly, quantitative yields are observed for 4-iodobenzoic acid, ~50% yields are noted for 3-iodobenzoic acid, and no product is detected for the 2-iodobenzoic acid, thus supporting the suggested variations in the interaction strength and catalytic affects of the substrate structure. Further evidence to support such an interaction for the 3-iodobenzoic acid species arises from the lower TOF values that are calculated; when compared to the 4-iodobenzoic acid TOFs, values of nearly half are observed, which could be indicative of the lower reactivity arising from the stronger interactions with the Pd nanomaterial surface.

While the inorganic morphology is likely to affect the individual interactions at the metallic surface, the full composite structure of the peptide-templated materials is likely to control the overall reactivity. As stated above, the peptide template presents a barrier that inhibits the reagents in solution from immediate contact with the Pd surface; the reagents must diffuse through the framework to reach and interact with the inorganic component. Furthermore, while the same concentration of Pd atoms is present in every reaction, the surface area for oxidative addition changes as the shape of the inorganic nanostructure varies. Together, these effects are likely to mediate the individual reactivity and result in the observations for the TOF values for the different materials as presented in Figure 2. For the Pd60 materials, the highest inorganic surface area is displayed; however, the penetration depth is likely to be the largest because of the high dispersity of the materials within the structure. Conversely, for the Pd120 NPNs, while the Pd surface area is likely to be the lowest of all the materials, the highest Pd loading occurs for these structures, thus pushing the reactive surface closer to the peptide/water interface to significantly minimize reagent diffusion. Together, one of these two criteria is maximized for the Pd60 or Pd120 samples; however, for the Pd90 materials, both of

these factors are minimized; thus, attenuation of the reactivity for the nanoribbons is possible. Specifically, for the Pd90 nanoribbons, the reactive surface area is decreased, as compared to the Pd60 nanoparticles, while the penetration depth is maximized, as compared to the Pd120 NPNs; thus, these two negative structural characteristics work in combination to minimize the reactivity for the Pd90 structures. This was previously shown for a single Stille reaction using 4-iodobenzoic acid;² however, as shown in Figure 2 and Table 1, such results are observed, on average, for all of the aryl halide reagents studied in the present analysis. While the trend is present, the error in the analysis precludes a direct correlation, but this is likely due to the leaching-based mechanism. For 4-iodobenzoic acid, Pd abstraction is more rapid because of the lack of surface adsorption of the acid group as discussed above; thus more reactive Pd species are released in a quicker fashion from the Pd60 and Pd120 materials because of the maximized surface area and penetration effects, respectively. As a result, higher catalytic turnover is expected over the time frame of the TOF studies, which is observed as higher values as compared to the Pd90 materials. When this abstraction process is slowed using the additional aryl halides, less Pd is released; thus, the TOF values for these systems is more dependent upon the released Pd rather than the initial abstraction process. As a result, slower TOFs are anticipated from the lower amount of Pd available for the reaction, which could generate the observed results that are closer in magnitude for all three materials. To more fully determine the structural affects of the materials for catalysis, a rapid reaction that occurs directly on the Pd surface, such as 4-nitrophenol reduction, is desirable. This would decouple the leaching process from the actual catalytic results thus amplifying the structural attributes of the materials for template-based reactivity.

Effects of the Peptide Template on Catalytic 4-Nitrophenol Reduction. While the Stille reaction appears to be dependent upon the structure of the materials, the proposed leaching mechanism could impact and/or minimize the effects to the catalytic reaction. To further confirm, characterize, and identify key structural elements that control the reactivity for template-based materials, it is important to study a separate class of catalytic reactions in which the mechanism is processed directly on the inorganic surface. To this end, the structural effects of templated materials could be amplified for surface-based reactions and can be used to further elucidate the structure/function relationship. For this, we have employed the reduction of 4-nitrophenol to 4-aminophenol using NaBH₄ that is catalyzed directly on the surface of noble metal nanomaterials dispersed in solution,^{52,53–59} where the overall reaction is presented in Scheme 2b.⁵⁶ This rapid reaction can be monitored using time-resolved UV–vis spectroscopy from which a full kinetics study can be completed. This will allow for a highly quantitative analysis of the nanomaterial structural effects of the various compositions of materials on the catalytic reactivity.

Figure 3a presents the UV–vis analysis of the 4-nitrophenol reduction reaction that is catalyzed using the Pd90 nanoribbons. Here, a Pd concentration of 79.0 μM and a temperature of 50.0 °C was employed to drive the reaction. Identical analyses were conducted in triplicate for all materials with the UV–vis spectra of the process presented in the Supporting Information, Figures S2–S7, for the Pd60 and Pd120 materials. For this reaction, the substrate, 4-nitrophenol, exhibits a strong absorbance peak at 400 nm under basic conditions.^{52,59} As this reagent is catalytically reduced by the Pd materials in the presence of a significant excess

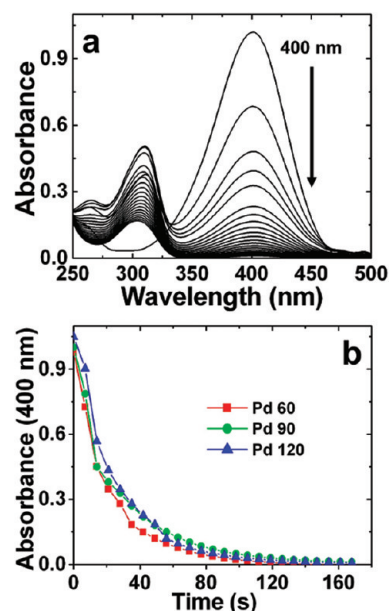


Figure 3. UV–vis analysis of the 4-nitrophenol reduction reaction. Part (a) displays the time-resolved UV–vis spectra used to extract kinetic information. The presented reaction was studied using the Pd90 nanoribbons at a temperature of 50.0 °C. Monitoring of a decrease in the absorbance at 400 nm, which arises from the 4-nitrophenol substrate, demonstrates a rapid decrease in intensity for all reactions studied, which is presented in part (b) for the Pd60, Pd90, and Pd120 materials at a reaction temperature of 50.0 °C.

of NaBH₄, the intensity of the 400 nm peak decreases and a new peak at 310 nm is generated corresponding to the 4-aminophenol final product.^{52,59} When a control reaction is performed in the absence of Pd, no change in the 400 nm peak is observed over the time frame of the study, indicating no reduction of the 4-nitrophenol substrate as shown in the Supporting Information, Figure S1, thus confirming the catalytic activity of the peptide-templated Pd nanomaterials. Note that an isosbestic point is not observed, which is likely due to two factors. First, the formation of H₂ gas bubbles during the reaction occurs, which can cause a minor degree of scattering.⁵⁹ Second, while 4-aminophenol is unambiguously produced, multiple intermediates are generated (Scheme 2b) that also absorb in this region. As previously demonstrated, kinetics studies for this reaction are thus completed using pseudo first order kinetics by monitoring the consumption of 4-nitrophenol as the concentration of NaBH₄, which is in significant excess, essentially remains constant.^{52,53–57} Figure 3b displays the diminishing values of the 400 nm intensity for the catalytic reduction reaction employing all three template-prepared materials over a time frame of 3.00 min. As anticipated, a rapid decrease in intensity is observed until the reaction is completed in ~2.00 min for all of the materials. Such results are consistent with previous noble metal nanomaterials for this reaction,^{52,53,58,59} suggesting that the present materials are highly active for the surface-based reaction.

Figure 4 presents the overall kinetic analysis of the 4-nitrophenol reduction reaction employing the template generated materials. To isolate the pseudo first order rate constant, k , eq 1 was used,⁵³

$$-kt = \ln\left(\frac{C_t}{C_0}\right) \quad (1)$$

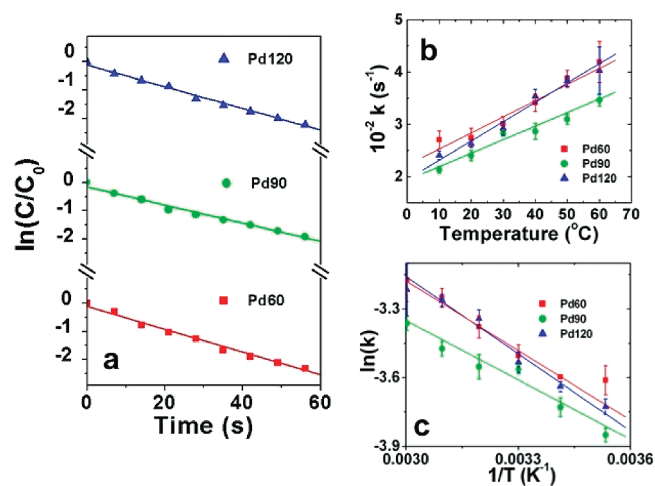


Figure 4. Kinetic analysis of the 4-nitrophenol reduction reaction employing the peptide-templated materials. Part (a) presents the pseudo first order kinetic plots for all of the materials studied at a reaction temperature of 50.0 °C. The slope of the best fit line represents the $-k$ value associated with each reaction. Part (b) presents the k -values for all of the catalytic systems as a function of temperature, which demonstrates an increase in k with an increase in temperature. Finally, part (c) displays the Arrhenius plots for each of the reaction systems, where the slope of the line is used to determine the E_a value.

where C_t represents the concentration of 4-nitrophenol at time t and C_0 represents the initial concentration of 4-nitrophenol at $t = 0.00$ min. Since the absorbance of the reagent is directly related to the concentration via Beer's law,⁶⁰ the absorbance intensities at the appropriate time points can be substituted to generate the plots of Figure 4a.^{53,57} Here, the $\ln((C_t)/(C_0))$ is plotted as a function of time, where the slope of the best fit line represents the $-k$ value of the reaction. For all three materials at the selected reaction conditions, triplicate reactions were completed where the R^2 value for all analyses was >0.90 .

To kinetically study the catalytic process, the reaction was monitored at 10.0 °C intervals between a temperature range of 10.0 and 60.0 °C employing all three nanoparticle morphologies. The average k -values for each system are presented graphically in Figure 4b and tabulated in Table 2. For all of the materials studied, the reaction temperature and rate constants were directly proportional such that as the temperature increased, the k -values also increased linearly. For instance, when the Pd60 nanospheres were studied at 10.0 °C, a rate constant of $0.027 \pm 0.002 \text{ s}^{-1}$ was observed that linearly increased to $0.042 \pm 0.004 \text{ s}^{-1}$ at 60.0 °C. When the Pd90 nanoribbons were used to drive the reaction, diminished k -values were observed that ranged from $0.021 \pm 0.001 \text{ s}^{-1}$ to $0.035 \pm 0.001 \text{ s}^{-1}$ over the temperature range. Finally, when the NPNs prepared in the Pd120 sample catalyzed the reaction, rate constants similar to the Pd60 materials were noted such that a k -value of $0.024 \pm 0.001 \text{ s}^{-1}$ was observed at 10.0 °C that increased to $0.040 \pm 0.005 \text{ s}^{-1}$ at 60.0 °C. These values are plotted in Figure 4b, which shows that while the Pd60 and Pd120 materials were able to catalytically drive the reaction at equivalent rates, the Pd90 materials demonstrated diminished rate constants over the entire range of the reaction temperatures. This suggests that the structures of the Pd60 and Pd120 materials are optimized to drive the surface-based reaction, while the Pd90 nanoribbons possess a structure that limits the reaction rate.

Table 2. Pseudo First Order Kinetic k -Values for the 4-Nitrophenol Reduction Reaction Employing the Pd60 Nanospheres, Pd90 Nanoribbons, and Pd120 NPNs

temperature	Pd Material [$10^{-2} k \text{ (s}^{-1}\text{)}$]		
	Pd60	Pd90	Pd120
10 °C	2.7 ± 0.2	2.1 ± 0.1	2.4 ± 0.1
20 °C	2.7 ± 0.2	2.4 ± 0.1	2.6 ± 0.1
30 °C	3.0 ± 0.1	2.8 ± 0.1	2.9 ± 0.1
40 °C	3.4 ± 0.2	2.9 ± 0.2	3.5 ± 0.1
50 °C	3.9 ± 0.2	3.1 ± 0.1	3.8 ± 0.1
60 °C	4.2 ± 0.4	3.5 ± 0.1	4.0 ± 0.5
$E_a \text{ (kJ/mol)}$	7.5 ± 0.9	7.2 ± 0.9	8.7 ± 1.2

Figure 4c presents the Arrhenius plot for all three-reaction systems from which the slope of the trend line can be used to determine the activation energy (E_a). From this analysis, E_a values of $7.5 \pm 0.9 \text{ kJ/mol}$, $7.2 \pm 0.9 \text{ kJ/mol}$, and $8.7 \pm 1.2 \text{ kJ/mol}$ were calculated for the 4-nitrophenol reduction reaction catalyzed by the Pd60 nanoparticles, Pd90 nanoribbons, and Pd120 NPNs, respectively, which are lower than values previously reported for other nanoparticle-based systems.^{57,58} From these energy values, which are strikingly very similar, it can be inferred that the energy required to drive the catalytic process is very similar for all of the materials studied. This is likely because in all three systems, zerovalent Pd is the catalytic agent and is present in all of the materials studied. The major difference, however, is the three-dimensional structure of the nanomaterials, which is likely mediating the process and could result in the observed variations in the catalytic rate constants.

The results from the 4-nitrophenol reduction reaction are fully consistent with the theory that reagent penetration depth and active surface area control the reactivity of the materials. When studying this process, the catalytic rate of the reaction was consistently lower for the Pd90 nanoribbons, while the Pd60 and Pd120 materials demonstrated higher rates. Furthermore, all three materials were calculated to possess equivalent E_a values; thus, they required the same amount of energy to drive the reaction. This suggests that the actual catalytic species in the process (Pd) is the same, but that the three-dimensional structure of the materials plays an important role in the reactivity. As discussed above, the substrates must diffuse through the peptide template to react at the catalytic materials such that those structures that position Pd closer to the solution interface would be inherently faster. To that end, the Pd120 NPNs that possess a more densely packed framework with inorganic components should drive the process at rapid rates, which is consistent with the observed data. In addition, it is clear that the quantity of surface area in solution also impacts the reaction rate. This is observed by the high k -values for the Pd60 nanospheres, which would present the highest inorganic surface area of all three systems. Finally, as with the Stille coupling, the Pd90 nanoribbons possess a diminished Pd surface area and a maximized penetration depth, as compared to the Pd60 and Pd120 materials, respectively, thus resulting in the lower k -values. Taken together, the quantitative kinetic analysis of the 4-nitrophenol reduction reaction strongly support these two structural factors, which was also suggested by the Stille results.

To probe these two structural effects, the following specific controls were studied. In Figure 5a, the 4-nitrophenol reduction

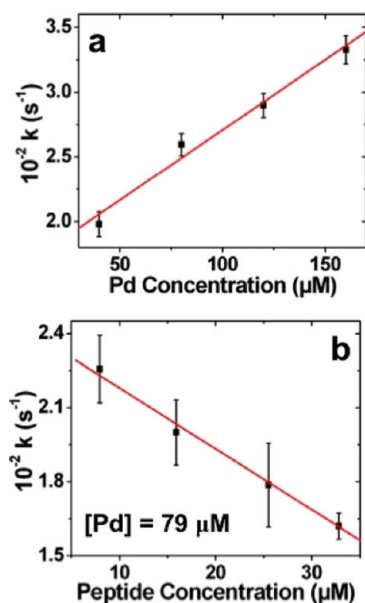


Figure 5. Control analysis of the structural effects of the peptide-templated nanocatalysts. Part (a) displays the effect of Pd concentration for the reduction reaction employing the Pd120 NPNs at room temperature. As is evident, as the amount of reactive surface area increases, the reaction rate increases. Part (b) presents the effect of reagent diffusion for the reduction reaction employing a constant concentration of the Pd60 nanospheres at room temperature with increasing concentrations of the R5 peptide template. Here, while the Pd concentration remains constant for all reactions, the concentration of empty peptide templates increases in solution, thus allowing for excess diffusion to occur to lower the reaction rate.

reaction was studied using increasing concentrations of the Pd120 NPNs. As the concentration of the Pd materials increased, the reaction rate also increased linearly. This control confirms that the catalytic surface area significantly affects the reaction such that greater surface areas facilitate a more rapid reaction. To probe the effect of reagent diffusion in the template, extra R5 peptide was added to the catalytic reaction employing a constant concentration of the Pd60 nanospheres. In this event, extraneous, metal free peptide frameworks would be present in solution into which the 4-nitrophenol molecules could diffuse. Those molecules that penetrate into the extraneous scaffolds would be inhibited from reacting with the catalyst until they were released from the empty template and subsequently diffused into a Pd-containing framework for catalytic turnover, thus lowering the rate constant. Indeed, as shown in Figure 5b, as the peptide concentration increased with a constant Pd60 concentration, the k -values for the reaction decreased, consistent with the diffusion-limited theory.

Additionally, these results suggest that both the inorganic surface area and the penetration depth play nearly equivalent roles in the reactivity of the materials. Should one of these structural considerations play a more significant part in the process, then a noticeable difference between the k -values of the Pd60 and Pd120 materials should have been observed. For instance, if the peptide template allowed for an excessively rapid diffusion process, and thereby negating this effect, then the availability of the inorganic surface area would likely become the limiting factor. Under such conditions, a linear decrease in the rate for the reduction reaction would be anticipated from the Pd60 nanospheres to the Pd120 NPNs, which should

demonstrate the smallest k -values. Conversely, if the template diffusion process was significantly impairing substrate diffusion to the point that it played a more significant role in the reactivity over the inorganic surface area, then the reaction rate for the Pd120 NPNs should be the greatest, with the smallest rates occurring for the more diffused and deeply packed Pd60 nanospheres. Interestingly, for both of the reactions studied that follow significantly different mechanisms, the Pd60 and Pd120 materials consistently demonstrate similar reactivity that is higher in magnitude than the average activity for the Pd90 structures. Taken together this suggests that the effects of active surface area and penetration depth work in combination to dictate the final reactivity of the biomimetic template-prepared nanomaterials.

SUMMARY AND CONCLUSIONS

In summary, the effects of the composite, three-dimensional structure of biomimetic template-prepared Pd nanomaterials has been studied for its effect on the catalytic reactivity. From this study, key structural criteria have been elucidated that directly affect the catalytic activity and the overall reaction rate. Here, both the metallic surface area and the penetration depth within the framework are demonstrated to play important roles in controlling the functionality. By having the unique ability to load selective amounts of Pd materials into the scaffolds, these two characteristics can be judiciously altered to probe these effects. This was observed via changes in the catalytic TOFs and reaction rates for Stille coupling and 4-nitrophenol reduction. As this trend was maintained for two reactions that follow drastically different catalytic mechanisms, this suggests that such structural effects may be applied to various different catalytic processes and may be maintained for other template-based nanostructures. The structure–function relationship of catalytic nanostructures is extremely important in order for the design and development of next generation systems that operate under ecologically friendly and energy efficient conditions. Such conditions are needed in light of the deteriorating global condition and diminishing natural resources.

ASSOCIATED CONTENT

S Supporting Information. Kinetic plots for the 4-nitrophenol reduction reactions and control at selected temperatures. This material is available free of charge via the Internet at <http://pubs.acs.org>.

AUTHOR INFORMATION

Corresponding Author

*Phone: (859) 257-3789. E-mail: mrkne2@email.uky.edu.

ACKNOWLEDGMENT

This material is based upon work supported by the National Science Foundation under Grant DMR-1005982. Furthermore, acknowledgement is made to the donors of the American Chemical Society Petroleum Research Fund for partial support of this research. The authors wish to thank L. Jackson and Professor B. C. Lynn for assistance with MALDI-TOF peptide characterization and M. Hazzard for graphical production assistance.

REFERENCES

- (1) Coppage, R.; Slocik, J. M.; Sethi, M.; Pacardo, D. B.; Naik, R. R.; Knecht, M. R. *Angew. Chem., Int. Ed.* **2010**, *49*, 3767.

- (2) Jakhmola, A.; Bhandari, R.; Pacardo, D. B.; Knecht, M. R. *J. Mater. Chem.* **2010**, *20*, 1522.
- (3) Pacardo, D. B.; Sethi, M.; Jones, S. E.; Naik, R. R.; Knecht, M. R. *ACS Nano* **2009**, *3*, 1288.
- (4) Scott, R. W. J.; Wilson, O. M.; Crooks, R. M. *J. Phys. Chem. B* **2005**, *109*, 692.
- (5) Bratlie, K. M.; Lee, H.; Komvopoulos, K.; Yang, P.; Somorjai, G. A. *Nano Lett.* **2007**, *7*, 3097.
- (6) Tsung, C.-K.; Kuhn, J. N.; Huang, W.; Aliaga, C.; Hung, L.-I.; Somorjai, G. A.; Yang, P. *J. Am. Chem. Soc.* **2009**, *131*, 5816.
- (7) Zhang, Y.; Grass, M. E.; Kuhn, J. N.; Tao, F.; Habas, S. E.; Huang, W.; Yang, P.; Somorjai, G. A. *J. Am. Chem. Soc.* **2008**, *130*, 5868.
- (8) Lee, Y. J.; Lee, Y.; Oh, D.; Chen, T.; Ceder, G.; Belcher, A. M. *Nano Lett.* **2010**, *10*, 2433.
- (9) Lee, Y. J.; Yi, H.; Kim, W.-J.; Kang, K.; Yun, D. S.; Strano, M. S.; Ceder, G.; Belcher, A. M. *Science* **2009**, *324*, 1051.
- (10) Nam, K. T.; Kim, D.-W.; Yoo, P. J.; Chiang, C.-Y.; Meethong, N.; Hammond, P. T.; Chiang, Y.-M.; Belcher, A. M. *Science* **2006**, *312*, 885.
- (11) Wang, L.; Yang, R. T. *Energy Environ. Sci.* **2008**, *1*, 268.
- (12) Varghese, O. K.; Paulose, M.; LaTempa, T. J.; Grimes, C. A. *Nano Lett.* **2009**, *9*, 731.
- (13) Jain, P. K.; Huang, X.; El-Sayed, I. H.; El-Sayed, M. A. *Acc. Chem. Res.* **2008**, *41*, 1578.
- (14) Seferos, D. S.; Giljohann, D. A.; Hill, H. D.; Prigodich, A. E.; Mirkin, C. A. *J. Am. Chem. Soc.* **2007**, *129*, 15477.
- (15) Rosi, N. L.; Mirkin, C. A. *Chem. Rev.* **2005**, *105*, 1547.
- (16) Rosi, N. L.; Giljohann, D. A.; Thaxton, C. S.; Lytton-Jean, A. K. R.; Han, M. S.; Mirkin, C. A. *Science* **2006**, *312*, 1027.
- (17) Astruc, D. *Inorg. Chem.* **2007**, *46*, 1884.
- (18) Daniel, M.-C.; Astruc, D. *Chem. Rev.* **2004**, *104*, 293.
- (19) Xia, Y.; Xiong, Y.; Lim, B.; Skrabalak, S. E. *Angew. Chem., Int. Ed.* **2009**, *48*, 60.
- (20) Garcia-Martinez, J. C.; Lezutekong, R.; Crooks, R. M. *J. Am. Chem. Soc.* **2005**, *127*, 5097.
- (21) Scott, R. W. J.; Wilson, O. M.; Oh, S.-K.; Kenik, E. A.; Crooks, R. M. *J. Am. Chem. Soc.* **2004**, *126*, 15583.
- (22) Wilson, O. M.; Knecht, M. R.; Garcia-Martinez, J. C.; Crooks, R. M. *J. Am. Chem. Soc.* **2006**, *128*, 4510.
- (23) Narayanan, R.; El-Sayed, M. A. *Langmuir* **2005**, *21*, 2027.
- (24) Mizugaki, T.; Murata, M.; Fukubayashi, S.; Mitsudome, T.; Jitsukawa, K.; Kaneda, K. *Chem. Commun.* **2008**, 241.
- (25) Eklund, S. E.; Cliffl, D. E. *Langmuir* **2004**, *20*, 6012.
- (26) Knecht, M. R.; Weir, M. G.; Frenkel, A. I.; Crooks, R. M. *Chem. Mater.* **2008**, *20*, 1019.
- (27) Knecht, M. R.; Weir, M. G.; Myers, V. S.; Pyrz, W. D.; Ye, H.; Petkov, V.; Buttrey, D. J.; Frenkel, A. I.; Crooks, R. M. *Chem. Mater.* **2008**, *20*, 5218.
- (28) Weir, M. G.; Knecht, M. R.; Frenkel, A. I.; Crooks, R. M. *Langmuir* **2010**, ASAP.
- (29) Scott, R. W. J.; Ye, H.; Henriquez, R. R.; Crooks, R. M. *Chem. Mater.* **2003**, *15*, 3873.
- (30) Ogasawara, S.; Kato, S. *J. Am. Chem. Soc.* **2010**, *132*, 4608.
- (31) Wang, S.; Wang, X.; Jiang, S. P. *Nanotechnology* **2008**, *19*, 455602.
- (32) Semagina, N.; Joannet, E.; Parra, S.; Sulman, E.; Renken, A.; Kiwi-Minsker, L. *Appl. Catal., A* **2005**, *280*, 141.
- (33) Song, Y.; Garcia, R. M.; Dorin, R. M.; Wang, H.; Qiu, Y.; Coker, E. N.; Steen, W. A.; Miller, J. E.; Shelnut, J. A. *Nano Lett.* **2007**, *7*, 3650.
- (34) Meric, P.; Yu, K. M. K.; Tsang, S. C. *Langmuir* **2004**, *20*, 8537.
- (35) Bernechea, M.; de Jesús, E.; López-Mardomingo, C.; Terreros, P. *Inorg. Chem.* **2009**, *48*, 4491.
- (36) Diallo, A. K.; Ornelas, C.; Salmon, L.; Aranzaes, J. R.; Astruc, D. *Angew. Chem., Int. Ed.* **2007**, *46*, 8644.
- (37) Ornelas, C.; Ruiz, J.; Salmon, L.; Astruc, D. *Adv. Synth. Catal.* **2008**, *350*, 837.
- (38) Chen, Y.-H.; Hung, H.-H.; Huang, M. W. *J. Am. Chem. Soc.* **2009**, *131*, 9114.
- (39) Knecht, M. R.; Pacardo, D. B. *Anal. Bioanal. Chem.* **2010**, 397, 1137.
- (40) Niu, Y.; Yeung, L. K.; Crooks, R. M. *J. Am. Chem. Soc.* **2001**, *123*, 6840.
- (41) Dickerson, M. B.; Sandhage, K. H.; Naik, R. R. *Chem. Rev.* **2008**, *108*, 4935.
- (42) Brutchey, R. L.; Morse, D. E. *Chem. Rev.* **2008**, *108*, 4915.
- (43) Slocik, J. M.; Govorov, A. O.; Naik, R. R. *Angew. Chem., Int. Ed.* **2008**, *47*, 5335.
- (44) Slocik, J. M.; Naik, R. R. *Adv. Mater.* **2006**, *18*, 1988.
- (45) Slocik, J. M.; Zabinsky, J. S.; Phillips, D. M.; Naik, R. R. *Small* **2008**, *4*, 548.
- (46) Kröger, N.; Deutzmann, R.; Sumper, M. *Science* **1999**, *286*, 1129.
- (47) Kröger, N.; Lorenz, S.; Brunner, E.; Sumper, M. *Science* **2002**, *298*, 584.
- (48) Knecht, M. R.; Wright, D. W. *Chem. Commun.* **2003**, *24*, 3038.
- (49) Espinet, P.; Echavarren, A. M. *Angew. Chem., Int. Ed.* **2004**, *43*, 4704.
- (50) Stille, J. K. *Angew. Chem., Int. Ed.* **1985**, *25*, 508.
- (51) Chan, W. C.; White, P. D. *Fmoc Solid Phase Peptide Synthesis: A Practical Approach*; Oxford Univ. Press: New York, 2000.
- (52) Pradhan, N.; Pal, A.; Pal, T. *Langmuir* **2001**, *17*, 1800.
- (53) Behrens, S.; Heyman, A.; Maul, R.; Essig, S.; Steigerwald, S.; Quintilla, A.; Wenzel, W.; Bürck, J.; Dgany, O.; Shoseyov, O. *Adv. Mater.* **2009**, *21*, 3515.
- (54) de Vries, J. G. *Dalton Trans.* **2006**, 421.
- (55) Reetz, M. T.; de Vries, J. G. *Chem. Commun.* **2004**, *14*, 1559.
- (56) Corma, A.; Concepción, P.; Serna, P. *Angew. Chem., Int. Ed.* **2007**, *46*, 7266.
- (57) Wunder, S.; Polzer, F.; Lu, Y.; Mei, Y.; Ballauff, M. *J. Phys. Chem. C* **2010**, *114*, 8814.
- (58) Zeng, J.; Zhang, Q.; Chen, J.; Xia, Y. *Nano Lett.* **2010**, *10*, 30.
- (59) Feng, Z. V.; Lyon, J. L.; Croley, J. S.; Crooks, R. M.; Vanden Bout, D. A.; Stevenson, K. J. *J. Chem. Educ.* **2009**, *86*, 368.
- (60) Skoog, D. A.; West, D. M.; Holler, F. J.; Crouch, S. R. *Fundamentals of Analytical Chemistry*, 8th ed.; Brooks Cole: New York, 2003.